A 3D Ultrasound Informed Model of Human Gastrocnemius Muscle

M Alipour[1], K Mithraratne[1], R.D. Herbert[2] and J Fernandez[1,3]

1. Auckland Bioengineering Institute, The University of Auckland, Auckland, NZ
2. Neuroscience Research Australia, Sydney, Australia
3. Department of Engineering Science, The University of Auckland, Auckland, NZ

Submitted as an **Original Article** to the Journal

Computer Methods in Biomechanics and Biomedical Engineering: Imaging & Visualization,

2015

Address correspondence to:

Justin W Fernandez

Auckland Bioengineering Institute

The University of Auckland, New Zealand

Email: j.fernandez@auckland.ac.nz

Phone: +64 9 373 7599 ext 89196

Running title: Finite element method, Gastrocnemius, Ultrasound, muscle mechanics, parameter optimisation

Abstract

Muscle fibre structure characterises muscle function, which in turn plays a key role in computer simulation of muscle shape. In this study we use 3D Ultrasound from human gastrocnemius muscle to identify and map the fibre orientation and deformation during passive motion in four subjects. This fibre description is integrated into a representative muscle volume element using a free-form deformation technique to create a muscle primitive that deforms according to the embedded muscle fibres within. For each subject we computed passive force that was used to optimise the constitutive behaviour so that the known deformation matched this load. Each subject was fit to match deformation at 25%, 50%, 75% and 100% of muscle stretch. The subjects that exhibited a larger fibre pennation angle change during passive stretch were characterised best by a more compliant constitutive law. In contrast, subjects that had a more parallel fibre deformation, showed stiffer behaviour. A whole gastrocnemius muscle built from these muscle primitives exhibited a contractile shape that is similar to that observed in human gastrocnemius contraction. This shape was evaluated against the same muscle embedded with fibres derived from diffusion weighted magnetic resonance imaging and was in good agreement. Muscle principal strain was shown to align with fibre direction and was spatially non-uniform. These muscle primitives may be used as building blocks to build large muscle volumes for mechanics simulation, visualisation and medical education.

Introduction

Ultrasound is a real-time imaging modality used widely to assess size and pennation of muscles such as in the quadriceps of young and old women [1] and *in vivo* pennation angle in human quadriceps [2]. Specific muscle fibre behaviour has also been evaluated including the relationships between muscle fibre size and angle [3], changes in pennation with joint angle and torque [4], prediction of tibialis anterior pennation angle changes during dorsiflexion [5]; and the *in vivo* human gastrocnemius architecture during rest and isometric contraction [6] of which is the focus of this study.

Cadaveric measurements of gastrocnemius fibre length and pennation is one possible option. However, Martins et al. [7] showed that cadaveric gastrocnemius fibre measurements differed from *in vivo* Ultrasound data by exhibiting fibre length and pennation changes between rest and fully contracted states. Hence, the motivation for this study was to develop finite element (FE) informed muscles from *in vivo* Ultrasound data. Ultrasound is also extendable to dynamic tasks including walking and running for the gastrocnemius [8]. Fascicle length and pennation angle measured using ultrasound has shown high reproducibility in treadmill walking [9] and treadmill running [10]. This ensures that the errors in fibre fields used to inform computational models are likely to be significantly less than using such modalities as DWI where data is typically integrated with more background and white noise [11, 12].

Muscle fibre architecture has been reported as a key factor in how well continuum computer models predict shape and force. For example, the detailed fibre architecture of the myocardium was reported by Nielsen et al. [13] who showed how contractile function is highly dictated by 3 microstructural directions. Material properties were fitted to the ‘pole-zero’ constitutive strain energy density function [14] which is also adopted in this study. Skeletal

muscle fibre distributions also play a key role in understanding physiological behaviour as part of multiscale models. Whole continuum muscle behaviour is highly influenced when homogenising substructural models that contain detailed muscle fibre descriptions [15]. Further, the orientation of muscle fascicles fitted to continuum FE models has been shown to explain the non-uniform strains observed in experiment [16].

Including fibres within a FE framework requires should not be linked to a specific element type but rather fitted to a mesh topology. One possible approach is to use a NURBS description and integrate this with FEM (Finite element model) for generic elements [17]. In this study we adopt a similar approach whereby a discrete fibre data set is fitted to a continuum field using a basis function that describes the element interpolation (from linear to cubic). Fibre directional vector is treated as a continuous field that may be applied to any element type. Basic building blocks serve as an efficient way to construct whole muscle volumes. For example a brick element basis with embedded fibres has been used to construct an entire cat gastrocnemius [18] and was shown to agree with experimental measurement of muscle deformations and force. Moreover, the concept of embedding digitised cadaver fibre fields into FE model primitives has been presented before [19], which can improve predicted force and contractile shape by up to 20% over simplified parallel fibre fields. In this study we extend this concept using 3D Ultrasound during passive deformation of the human gastrocnemius.

In this study we present a FE muscle primitive derived using 3D ultrasound data of human gastrocnemius muscle. The model is developed for four subjects to predict deformation in a representative volume of interest (a muscle element primitive) as part of a FE analysis. For each subject the passive tension was measured and combined with the fascicular data to determine subject-specific passive constitutive muscle parameters. The model was fit to 25%,

50%, 75% and 100% muscle deformation for each subject. A whole gastrocnemius muscle is built from these muscle primitives to highlight usability. Contractile mechanics simulations are run to observe predicted surface shape. Ultrasound informed muscle shape is compared with an equivalent geometrical model informed with fibres derived from DWI. Spatial muscle strain is also characterised.

Methods

Experiment

The ultrasound data used in this study are a subset of data that have been reported elsewhere [20]. Four subjects (mean age 24.6 ± 5.2, mean weight 60.6 ± 10.8 kg, mean height 171.6 ± 6.4 cm) had 3D Ultrasound collected during a passive seated knee flexion task (full subject details in Table 1).

The knee was flexed about 79 ± 6.7˚ and the subject configuration is shown in Figure 1. No subjects had any musculoskeletal disorders. Ethical approval was obtained from the South Eastern Sydney Local Health District Human Research Ethics Committee. The left foot was placed on a dynamometer foot plate (Cybex Norm with Humac, CSMi, Stoughton, MA, USA) and the ankle was rotated from fully plantarflexed to a fully dorsiflexed. Ankle rotation was slow (5 degrees/second) as slow speed stretches are unlikely to evoke muscle stretch reflexes, so the muscle is more likely to be passive. Surface EMG was used to confirm that the ankle plantarflexor muscles were relaxed. Two Ultrasound transducers (Esaote MyLab25 with LA522E 46 mm linear array, 7.5–12 MHz operating at 12 MHz; Esaote, Genoa, Italy) were used synchronously to image the gastrocnemius over the core muscle belly with a field of view of 110 mm. The location and orientation of the ultrasound image in leg space was determined using an

optical 3D motion analysis system. For full ultrasound experiment protocols see the work of Herbert et al. (2015) [20]. The muscle tension T_m in the gastrocnemius was obtained using the method described by Hoang and colleagues [21, 22]. T_m is related to muscle length by Equation 1,

$$T_m = \frac{1}{\alpha_G} e^{\alpha_G (lg - lgs)}, \quad (1)$$

where α_G is a constant, found by optimisation, that determines the stiffness of the muscle and is referred to as the "stiffness index" [21]. *lg* is the muscle length and *lgs* the muscle slack length. For all the forces collected, see table 2 and table 3.

Finite Element Model

For each subject a set of muscle fibres was digitised by identifying the 3D coordinates of the fibres' origins and insertions into the tendon. Figure 2 shows this process for a single slice from the 3D Ultrasound set identifying a segmented fibre at 0% elongation. This is repeated for nine fibres with the proximal and distal insertions shown as spheres. Finally, the fibres are embedded inside a three-element host mesh, which represents the basic muscle primitive in this study. We adopted a free form deformation technique to pass the measured fibre deformation to the muscle element primitive. In this approach the deforming fibres are replaced by an element that deforms based on underlying fibre movement. The particular method used is called 'host-mesh' fitting [23] and is illustrated in Figure 3 where three representative fibres in green at baseline with corresponding proximal and distal landmarks are morphed to match the same fibres in red at 100% elongation. The fibres are embedded inside a three-element host, which is morphed so as to minimise the distance between green landmarks and red targets. In order to

solve this we employ an iterative closest point algorithm to solve a least squares minimisation. The objective function that is minimised is:

$$F(u_n) = \sum_{d=1}^{N} W_d \, ||u(\xi_{1d}, \xi_{2d}, \xi_{3d}) - z_{3d}||^2 + F_s(u_n), \quad (2)$$

where z_d are the geometric coordinates of the target points for the muscle fibre d, w_d is a weighting for each control point, $u(\xi_{1d}, \xi_{2d}, \xi_{3d})$ are the landmark points interpolated at the finite element material coordinates $(\xi_{1d}, \xi_{2d}, \xi_{3d})$ and $F_s(u_n)$ is the Sobolev smoothing penalty function [11] used to constrain the motion of the deforming host by placing weights on the curvature, arc length, area and volume measures. The second order Sobelov penalty function used is:

$$F_s(u_n) = \iiint_0^1 \left\{ \alpha_1 \left\| \frac{\partial u}{\partial \xi_1} \right\| + \alpha_2 \left\| \frac{\partial u}{\partial \xi_2} \right\| + \alpha_3 \left\| \frac{\partial u}{\partial \xi_3} \right\| + \alpha_4 \left\| \frac{\partial^2 u}{\partial \xi_1^2} \right\|^2 + \alpha_5 \left\| \frac{\partial^2 u}{\partial \xi_2^2} \right\|^2 + \alpha_6 \left\| \frac{\partial^2 u}{\partial \xi_3^2} \right\|^2 + \right.$$
$$\left. \alpha_7 \left\| \frac{\partial^2 u}{\partial \xi_1 \partial \xi_2} \right\|^2 + \alpha_8 \left\| \frac{\partial^2 u}{\partial \xi_2 \partial \xi_3} \right\|^2 + \alpha_9 \left\| \frac{\partial^2 u}{\partial \xi_3 \partial \xi_1} \right\|^2 + \alpha_{10} \left\| \frac{\partial^3 u}{\partial \xi_1 \partial \xi_2 \partial \xi_3} \right\|^2 \right\} d\xi_1 \, d\xi_2 \, d\xi_3, \quad (3)$$

where each Sobolev weight, $\alpha_i (i=1..5)$, has its own magnitude dependent effect on a particular characteristic shape of the host fitted object; α_1, α_2 and α_3 restrict the arc-length; α_4, α_5 and α_6 regulate the arc-curvature; α_7, α_8, α_9 represents the face area; and α_{10} represents the volume of the host in the ξ_1, ξ_2, ξ_3 directional space, respectively. For this study we placed a minimal weight of 0.001 on α_1 (arc-length in the longitudinal direction), higher weight of 0.01 on α_2 and α_3 (arc-length in the transverse directions), no weights on the arc-curvature or element face area and a strong weight of 0.01 on α_{10} to constrain the volume change in the element.

A structurally based orthotropic constitutive law previously used for passive cardiac [24] and skeletal muscle [23] , the ‘pole-zero‘ relation [25] was adopted and is defined in Equation 4.

$$W = k_{\alpha\beta} \frac{E_{\alpha\beta}^2}{\left| a_{\alpha\beta} \quad E_{\alpha\beta} \right|^{b_{\alpha\beta}}} \tag{4}$$

where the strain energy density function, W, is defined by an asymptote function with $k_{\alpha\beta}$ the scaling function, $b_{\alpha\beta}$ curvature control, $a_{\alpha\beta}$ a strain limiting pole and $E_{\alpha\beta}$ the Green's strain components. The model was treated as transversely isotropic with the fibre direction $\alpha=\beta=1$ aligned to the fibre orientation from Ultrasound images. After choosing an initial guess for the 'pole-zero' parameters we used the 'fmincon' function in the Matlab Optimisation Toolbox [26] to optimally choose parameters that minimised the difference between the measured muscle force and the computed force. This was performed until the RMS error was less than 0.01 N (or 0.58 ± 0.19% error across all subjects). For this study we optimised the pole ($a_{\alpha\beta}$) in the fibre direction, which was the most sensitive parameter and fixed the scaling ($k_{\alpha\beta}$) and curvature ($b_{\alpha\beta}$) parameters. The curvature was set to 1.0 and scaling coefficient set to 0.1 MPa based on previous experience with cardiac [25] and skeletal tissues [23]. We set a bound on the solution space for $a_{\alpha\beta}$ as 0.01 to 5.0. An initial guess was obtained from trials based on previous skeletal muscles [23].

Muscle deformation was solved using the weak form of the governing equation for finite elastic mechanics in CMISS (www.cmiss.org) and is given by:

$$\int_{V_o} \frac{1}{J} T^{\alpha\beta} F_\beta^j \frac{\partial \delta u_j}{\partial \upsilon_\alpha} dV_o = 0 , \tag{5}$$

since the gastrocnemius muscle primitive is undergoing large strain (greater than 10%). V_o is the undeformed volume and δu_j is the virtual displacement and $F_\beta^j = \partial x_j / \partial \upsilon_\beta$ is the deformation gradient tensor which maps between the deformed spatial coordinates x_j and material

coordinates, υ_β. The Jacobian, *J*, is the determinant of the deformation gradient tensor, *F* and $T^{\alpha\beta}$ is the 2nd Piola-Kirchoff stress tensor,

$$T^{\alpha\beta} = \frac{\partial W}{\partial E_{\alpha\beta}} + p a_\upsilon^{\alpha\beta}, \tag{6}$$

and defined with respect to an undeformed orthogonal curvilinear material coordinate system, ν_α. *W* is the 'pole zero' strain energy density function and $E_{\alpha\beta}$ are the Green-Lagrange strain components. The hydrostatic pressure, *p*, arises in order to satisfy muscle volume conservation. The contravariant metric tensor $a_\upsilon^{\alpha\beta} = \partial\upsilon_\alpha / \partial x_k . \partial\upsilon_\beta / \partial x_k$ is the inverse of the right Cauchy deformation tensor (covariant metric tensor).

Results

Passive fibre deformation during gastrocnemius stretch was passed to a representative continuum element, as shown in figure 4 (subject 1). Following optimisation of the fibre end points to match 25% to 100% of muscle stretch the deformed host shape was predicted and the volume of the element did not change by more than 1%. Figure 5 shows another example where the subject has a higher pennation movement during stretch (subject 4). In this scenario, the deformed host is stretched further longitudinally and is more compliant. The average RMS error between landmark and target fibres was at most 2 mm in all host mesh deformations.

The constitutive law was fit for all four subjects and is shown in Figure 6 with parameters given in Table 4. The subjects that exhibited a larger fibre pennation change during passive stretch were best characterised by a more compliant constitutive law (shown for subjects 2 and 4). In contrast, subjects that had a more parallel fibre deformation, showed a stiffer behaviour

(shown for subjects 1 and 3). The transverse directions (labelled as sheet and sheet-normal) were elastically less stiff than all fibre directions.

An entire gastrocnemius muscle was built from these muscle primitives and the entire muscle field is shown in Figure 7. There was a clear bi-pennate characterisation for the whole continuum with fibres merging towards a central tendon. A finite elastic mechanics simulation using a Hill type contraction model produced a distinct bulge on the medial head of the gastrocnemius (the larger head) and a distinct crease formed between the heads, shown in Figure 8. An axial view highlighted the effect of the fibres contracting inwards towards the central tendon. To evaluate this behaviour we compared this with the same muscle fitted with diffusion weighted derived fibres under the same level of contraction and the resulting muscle profile was highly consistent. However, the diffusion derived model did show more distinct creasing and bulging than the Ultrasound model from this study. Comparison between the two models showed an RMS error difference in shape of 8.8 mm. (Figure 9)

Muscle strain was shown to align with fibre direction and was spatially non-uniform as shown in Figure 10. The strain is viewed from the posterior and axial views and is split into maximum principal compressive and tensile strain separately to reveal the spatially varying behaviour in 3D. Figure 10 (left) reveals a maximum compressive principal strain in the muscle centre towards the central tendon up to a peak strain of 0.24 (24% ε). Figure 10 (right) reveals a maximum tensile principal strain on the medial outer side towards the larger medial head up to a peak strain of 0.1 (10% ε). Strain was highest in the medial and lateral heads and lowest near the proximal lateral region closest to the femoral insertion site.

Discussion

The study developed a muscle primitive using 3D Ultrasound in the human gastrocnemius from four subjects as a representation of a bipennate muscle. The extracted 3D Ultrasound fibre data were embedded inside a representative muscle volume element that captured approximately 4 cm x 2 cm x 2 cm of the muscle belly and morphed to match the moving fibre field imaged from 3D Ultrasound using a free form deformation technique called 'host-mesh' fitting. This produced a series of known muscle shapes (that matched the underlying fibre data) and we mechanically simulated these known displacements in order to match the measured muscle force by optimising material properties. The 'pole-zero' parameters were optimised to match four positions in the data (25%, 50%, 75% and 100%) of the experimental passive muscle stretch with an average fitting error of less than 1% of the force. It was shown that the whole continuum muscles produced a realistic contractile shape when simulated, which was comparable with a diffusion weighted derived model reported by Fernandez et al. [27] . Mechanical simulation showed spatially varying non-uniform strain that aligned with the complex fibre orientation. Compressive strain was highest in the central belly of the muscle and tensile strain was highest in the outer medial head. These muscle primitives are being developed as part of the Physiome repository [28] and the Musculoskeletal Atlas Project (MAP) [29] in order for people to adopt and fit to subject-specific data.

There are a number of limitations in this study that should be considered when interpreting the results. Firstly, the range of muscle lengths was much less than the full physiological range of lengths. That was because (a) the Ultrasound transducers could not be placed behind the knee when the knee was fully flexed, (b) it was not possible to simultaneously extend the knee and dorsiflex the ankle, so we just dorsiflexed the ankle and (c) most markers

were visible for some but not all of the movement so we selected a subset of markers that were available for a common block of frames. This meant dropping many frames at the beginning and the end of the movement. Secondly, when developing the volume elements we selected only 9-12 fibres per muscle primitive to describe the entire behaviour of this region. This passive deformation may have been improved if more fibre data were available. We evaluated this possible limitation by fitting a muscle volume with 9 and 12 fibres and found that the overall deformation did not vary significantly as long as the fibres covered the entire block uniformly. Thirdly, the optimisation was sensitive to the initial parameter set, which was selected based on previous skeletal muscles fitted to the 'pole-zero' constitutive law. We did, however, try small variations of the initial guess and the model converged to the same solution as long as the initial guess was not too far out of range.

The fitted material properties were stiffer in the fibre direction and it was shown that the two subjects with the larger pennation angle change during deformation produced a less stiff strain energy density function, characterised by a larger pole in the 'pole-zero' law. In contrast, the two subjects that showed less pennation change during deformation exhibited a stiffer strain energy density function, characterised by a smaller pole in the 'pole-zero' law. These results provide a range of likely constitutive parameters that can describe healthy subjects. In addition to developing a useful muscle building block we also aimed to characterise stress-strain behaviour of healthy muscles. This initial result provides a basis for future comparison with pathologic muscles such as the muscles of people with contracture after stroke, spinal cord injury or cerebral palsy.

We showed that using the muscle primitive to build a complete gastrocnemius muscle fitted to a new subject worked effectively. Specifically, we were able to simulate active

contraction using a previously presented version of the Hill type model (see Appendix A) and this produced a shape and strain pattern that was consistent with what had been previously reported using DWI based fibres in humans [27]. However, the diffusion weighted muscle produced a deeper crease between the lateral and medial heads showing an RMS geometric difference in shape of close to 1 cm (Figure 9). Nevertheless, both ultrasound and DWI produced fibre orientations that were similar spatially. Specifically, the high compressive strain in the central muscle region between the medial and lateral heads and the high tensile strain on the outer larger medial head was also reported in the diffusion imaging study [27]. The highly non-uniform strain pattern is consistent with previous FE models that report non-uniform patterns due to fibre orientation [16, 30]. Furthermore, the range of predicted strain up to 0.24ε is consistent with the FE prediction due to active contraction in [30].

It was observed that the benefit of modelling muscle volume at the chose scale was that all the fibre and fibre connection behaviour is captured in the one muscle primitive. If we were to model at the fibre level, we would also require models of the fibre connective tissue. Hence, the scale of the representative muscle element is highly suitable as a building block for whole muscles without being concerned about multiscale methods, which is more computationally challenging. This study has shown that Ultrasound is a useful imaging modality for capturing real-time fibre change. Future uses of this data include characterising healthy versus pathologic muscle and creating a table of material parameters for patients with different age and health conditions to be used for mechanics and graphical representation.

References:

1. Young, A., M. Stokes, and M. Crowe, *Size and strength of the quadriceps muscles of old and young women*.* European journal of clinical investigation, 1984. **14**(4): p. 282-287.
2. Rutherford, O. and D. Jones, *Measurement of fibre pennation using ultrasound in the human quadriceps in vivo.* European journal of applied physiology and occupational physiology, 1992. **65**(5): p. 433-437.
3. Henriksson-Larsen, K., et al., *Do muscle fibre size and fibre angulation correlate in pennated human muscles?* European journal of applied physiology and occupational physiology, 1992. **64**(1): p. 68-72.
4. Herbert, R. and S. Gandevia, *Changes in pennation with joint angle and muscle torque: in vivo measurements in human brachialis muscle.* The Journal of Physiology, 1995. **484**(Pt 2): p. 523-532.
5. Maganaris, C.N. and V. Baltzopoulos, *Predictability of in vivo changes in pennation angle of human tibialis anterior muscle from rest to maximum isometric dorsiflexion.* European journal of applied physiology and occupational physiology, 1999. **79**(3): p. 294-297.
6. Narici, M., et al., *In vivo human gastrocnemius architecture with changing joint angle at rest and during graded isometric contraction.* The Journal of Physiology, 1996. **496**(Pt 1): p. 287-297.
7. Martin, D., et al., *Comparing human skeletal muscle architectural parameters of cadavers with in vivo ultrasonographic measurements.* Journal of ANATOMY, 2001. **199**(04): p. 429-434.

8. Lichtwark, G.A., K. Bougoulias, and A. Wilson, *Muscle fascicle and series elastic element length changes along the length of the human gastrocnemius during walking and running.* Journal of biomechanics, 2007. **40**(1): p. 157-164.

9. Aggeloussis, N., et al., *Reproducibility of fascicle length and pennation angle of gastrocnemius medialis in human gait in vivo.* Gait & posture, 2010. **31**(1): p. 73-77.

10. Giannakou, E., N. Aggeloussis, and A. Arampatzis, *Reproducibility of gastrocnemius medialis muscle architecture during treadmill running.* Journal of Electromyography and Kinesiology, 2011. **21**(6): p. 1081-1086.

11. Landman, B.A., P.-L. Bazin, and J.L. Prince, *Estimation and application of spatially variable noise fields in diffusion tensor imaging.* Magnetic resonance imaging, 2009. **27**(6): p. 741-751.

12. Koltchinskii, V., L. Sakhanenko, and S. Cai, *Integral curves of noisy vector fields and statistical problems in diffusion tensor imaging: Nonparametric kernel estimation and hypotheses testing.* The Annals of Statistics, 2007: p. 1576-1607.

13. Nielsen, P., et al., *Mathematical model of geometry and fibrous structure of the heart.* American Journal of Physiology-Heart and Circulatory Physiology, 1991. **260**(4): p. H1365-H1378.

14. Hunter, P.J., *Myocardial constitutive laws for continuum mechanics models of the heart.* Advances in experimental medicine and biology, 1995. **382**: p. 303.

15. Röhrle, O., J.B. Davidson, and A.J. Pullan, *A physiologically based, multi-scale model of skeletal muscle structure and function.* Frontiers in physiology, 2012. **3**.

16. Blemker, S.S., P.M. Pinsky, and S.L. Delp, *A 3D model of muscle reveals the causes of nonuniform strains in the biceps brachii.* Journal of biomechanics, 2005. **38**(4): p. 657-665.

17. Lu, Y., et al., *Modelling skeletal muscle fibre orientation arrangement.* Computer methods in biomechanics and biomedical engineering, 2011. **14**(12): p. 1079-1088.

18. Lemos, R., et al., *A framework for structured modeling of skeletal muscle.* Computer methods in biomechanics and biomedical engineering, 2004. **7**(6): p. 305-317.

19. Sánchez, C.A., et al., *Embedding digitized fibre fields in finite element models of muscles.* Computer Methods in Biomechanics and Biomedical Engineering: Imaging & Visualization, 2014. **2**(4): p. 223-236.

20. Herbert, R., et al., *Changes in the length and three-dimensional orientation of muscle fascicles and aponeuroses with passive length changes in human gastrocnemius muscles.* The Journal of Physiology, 2015. **593**(2): p. 441-455.

21. Kwah, L.K., et al., *Passive mechanical properties of gastrocnemius muscles of people with ankle contracture after stroke.* Archives of physical medicine and rehabilitation, 2012. **93**(7): p. 1185-1190.

22. Hoang, P., et al., *A new method for measuring passive length–tension properties of human gastrocnemius muscle in vivo.* Journal of biomechanics, 2005. **38**(6): p. 1333-1341.

23. Ateshian, G.A., et al., *Computational modeling of chemical reactions and interstitial growth and remodeling involving charged solutes and solid-bound molecules.* Biomechanics and modeling in mechanobiology, 2014: p. 1-16.

24. Hunter, P., A. McCulloch, and H. Ter Keurs, *Modelling the mechanical properties of cardiac muscle.* Progress in biophysics and molecular biology, 1998. **69**(2): p. 289-331.

25. Hunter, P., S. Sideman, and H. Fozzard, *Myocardial constitutive laws for continuum mechanics models of the heart.* Advances in experimental medicine and biology, 1995. **382**: p. 303-318.

26. Babarenda Gamage, T.P., et al., *Identification of mechanical properties of heterogeneous soft bodies using gravity loading.* International journal for numerical methods in biomedical engineering, 2011. **27**(3): p. 391-407.

27. J Fernandez, M.A., K Mithraratne *A diffusion tensor informed model of the human gastrocnemius muscle.* IEEE Transactions in Biomedical Engineering, 2015. **In Review**.

28. Fernandez, J., et al., *Modelling the passive and nerve activated response of the rectus femoris muscle to a flexion loading: a finite element framework.* Medical engineering & physics, 2005. **27**(10): p. 862-870.

29. Zhang, J., et al., *The MAP Client: User-Friendly Musculoskeletal Modelling Workflows*, in *Biomedical Simulation*2014, Springer. p. 182-192.

30. Chi, S.-W., et al., *Finite element modeling reveals complex strain mechanics in the aponeuroses of contracting skeletal muscle.* Journal of biomechanics, 2010. **43**(7): p. 1243-1250.

31. Hunter, P.J., *Myocardial constitutive laws for continuum models of the heart*, in *Molecular and subcellular cardiology*, B.R. Sidman S, Editor 1995: New York:. p. 303-318.

32. Hunter, P.J., *Myocardial constitutive laws for continuum mechanics models of the heart*, in *Molecular and subcellular cardiology*1995, Springer. p. 303-318.

Appendix A

For muscle contraction we used the model of Hunter [24] and added a contractile force in the DWI informed fibre direction to simulate muscle action given by:

$$\sigma_0(\lambda, Ca_{actn}) = \frac{(Ca_{actn}.[Ca^{2+}]_{\max})^h}{(Ca_{actn}.[Ca^{2+}]_{\max})^h + (c_{50})^h}.\sigma_{ref}[1+\beta(\lambda-1)], \quad \text{(A1)}$$

where σ_0 is the active tension added to the fibre direction and given by the calcium-tension derived from the 'fading-memory' model, which is based on the Hill type model [31, 32]. Ca_{actn} is the level of activation (non-dimensional calcium value), λ is the sarcomere stretch, $[Ca^{2+}]_{\max}$ is the intracellular calcium concentration for maximum activation, c_{50} is the concentration at which isometric tension is 50% of its maximum, h is the Hill coefficient, T_{ref} is the active isometric tension when $\lambda = 1$ and β is the slope parameter.

Figures:

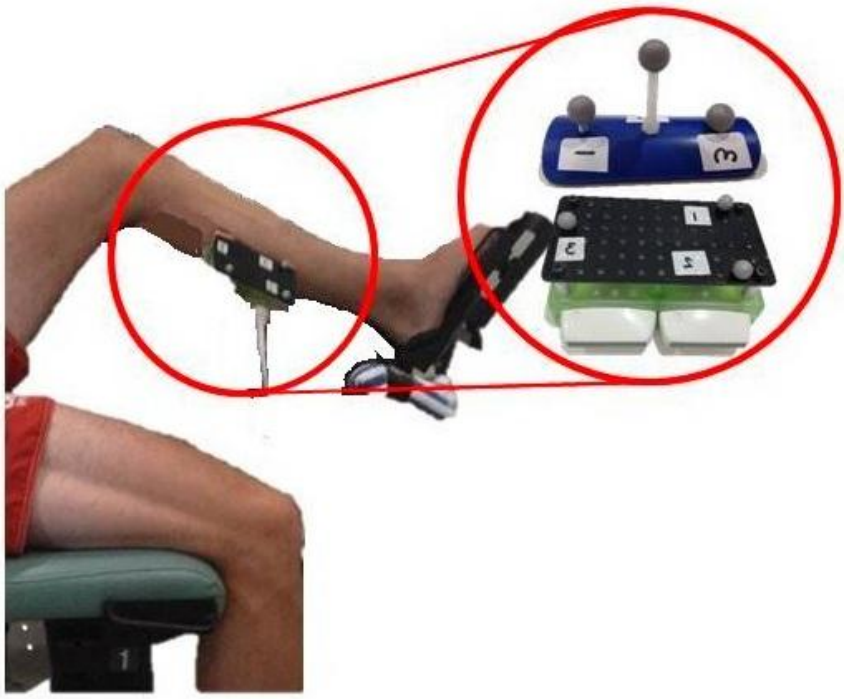

Figure 1: The experiment setup. Each subject was seated with the leg in a flexed pose and the foot was moved through dorsiflexion. Top right shows the triad of markers attached to the leg used to define the leg frame of reference. Markers are also attached to the ultrasound transducer to define the imaging plane.

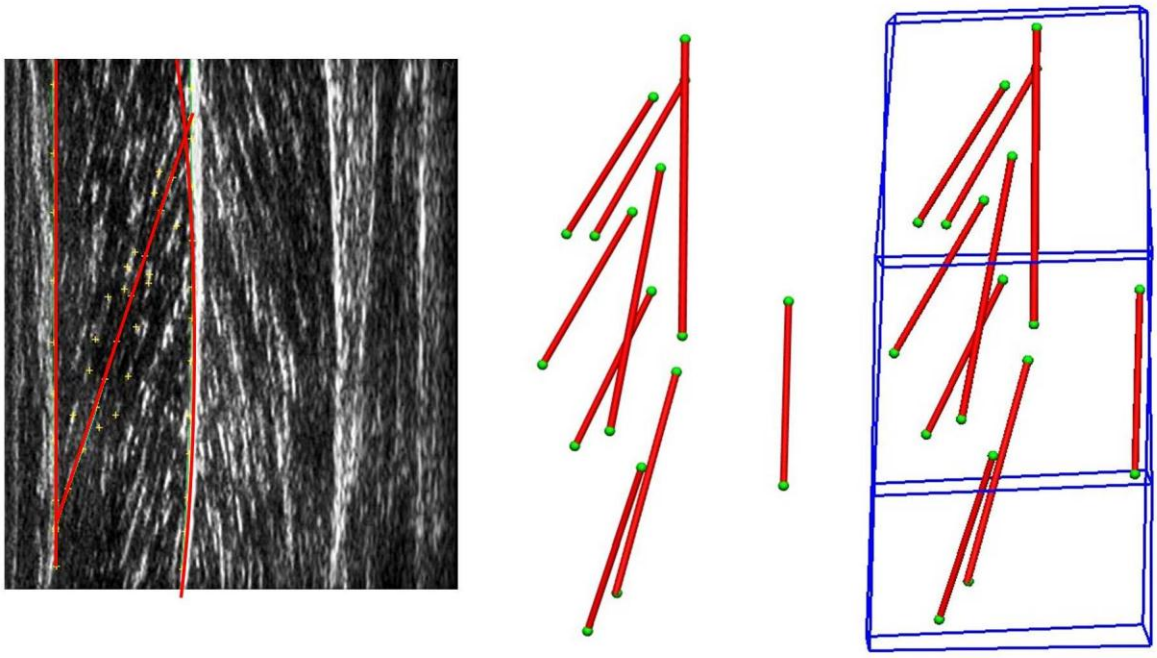

Figure 2: (Left) is a slice from the 3D Ultrasound image identifying a manually segmented fibre at time zero; (Middle) is a 2D representation of a 3D set of nine segmented fibres shown as red lines. Green circles are the proximal and distal insertions; (Right) shows the fibres embedded inside a three-element 3D host mesh for the same volume of interest

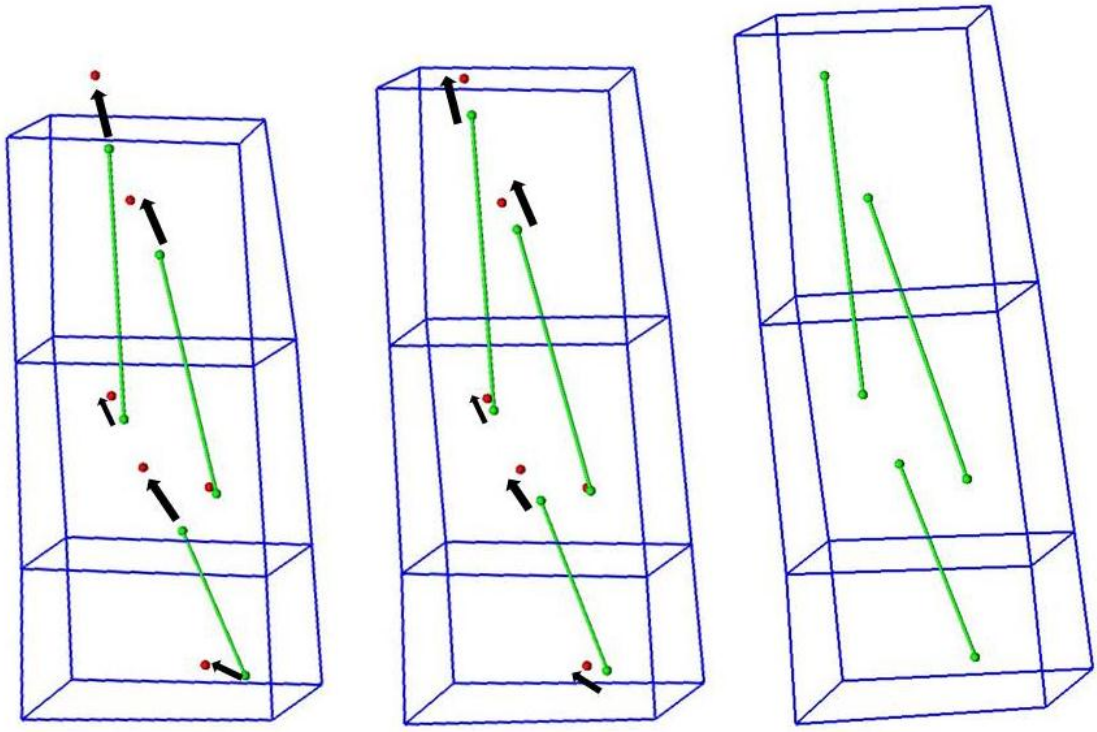

Figure 3: Free-form deformation pipeline: (Left) shows three representative fibres in green at baseline with corresponding proximal and distal landmarks at 100% elongation shown in red. The fibres are embedded inside a 3-element host. (Middle) shows the deformation of the host at 50% elongation driven by the baseline fibres in order to match the target proximal and distal fibre endpoints. (Right) shows the deformation of the host at 100% fibre elongation and perfectly matched to the target fibres.

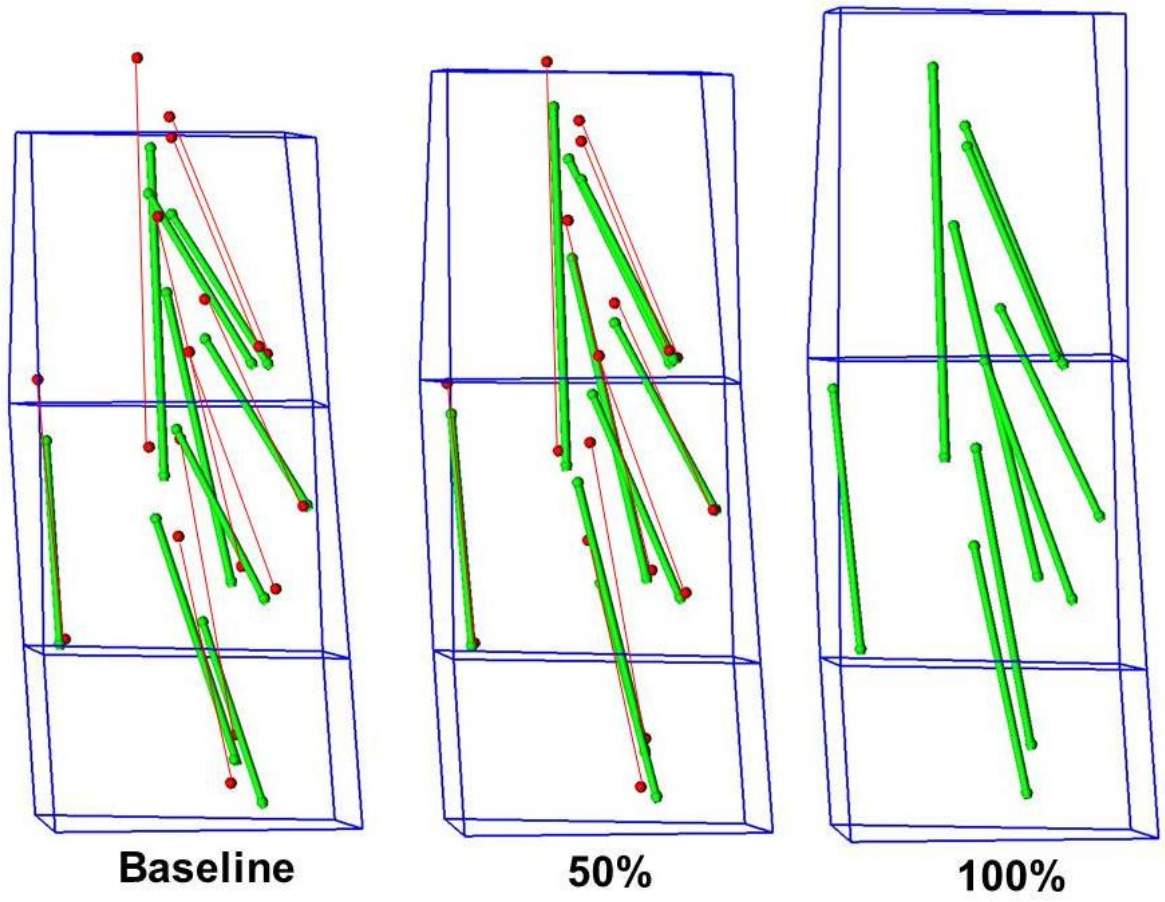

Figure 4: Free form deformation of subject 1 highlighting the matching of all baseline fibres to the fibre locations at 100% elongation. This produces a deformed host whose shape minimises the difference between baseline and target fibres.

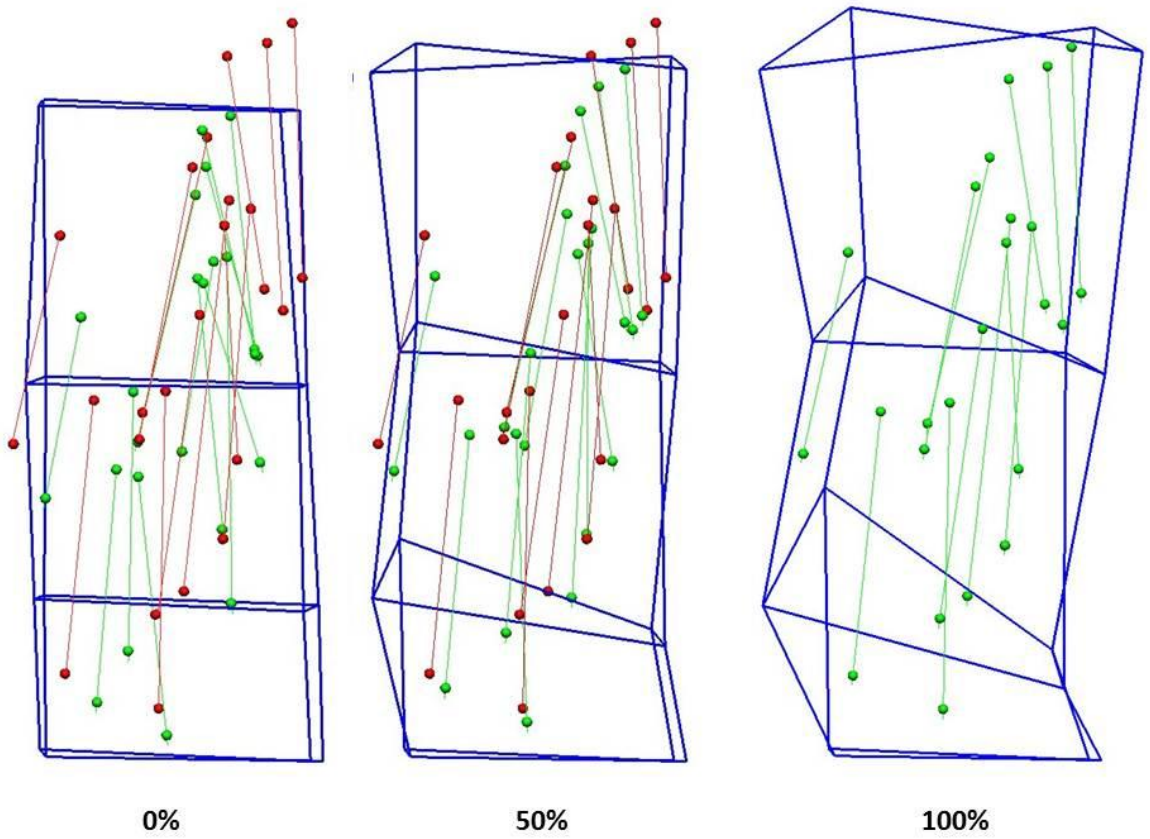

Figure 5: Free form deformation of subject 4 (who has a higher pennation change during stretch) highlighting the matching of all baseline fibres to the fibre locations at 100% elongation. This produces a deformed host whose shape minimises the difference between baseline and target fibres.

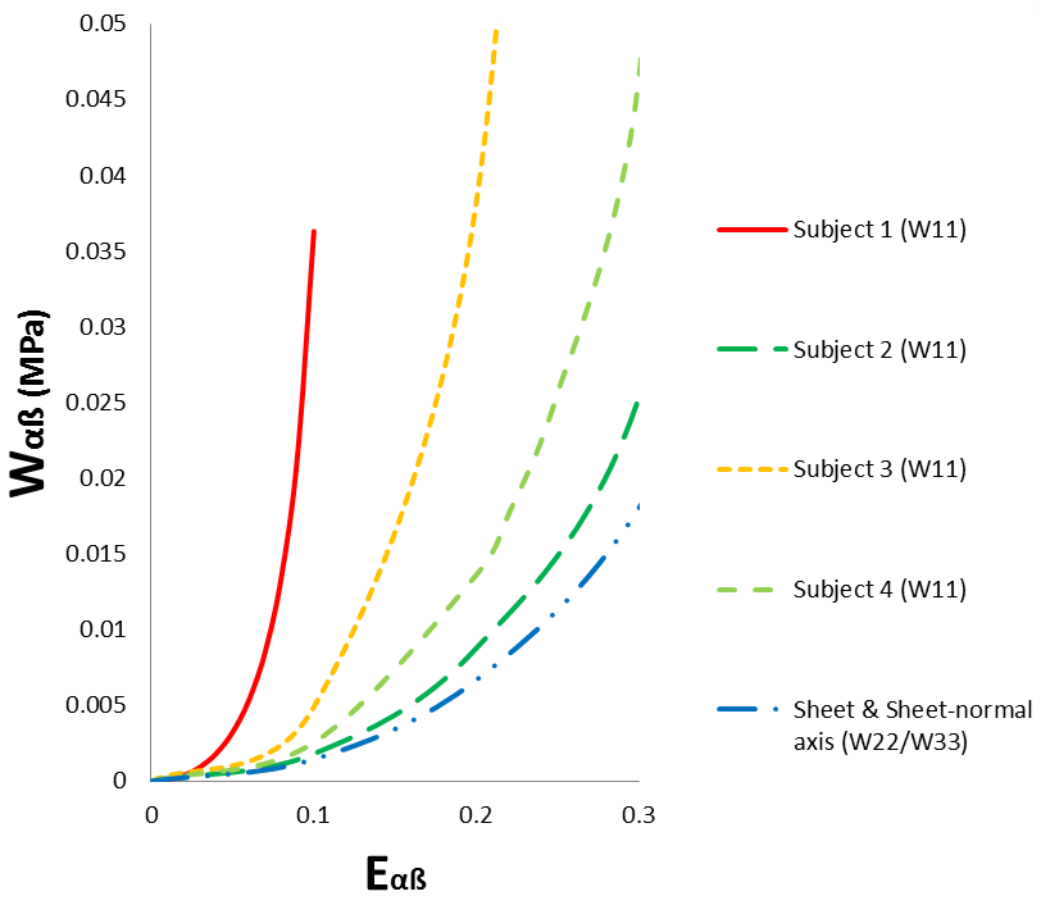

Figure 6: Fitted pole-zero constitutive law strain energy density for subjects one to four in the fibre direction (W11) and transverse directions (W22/W33).

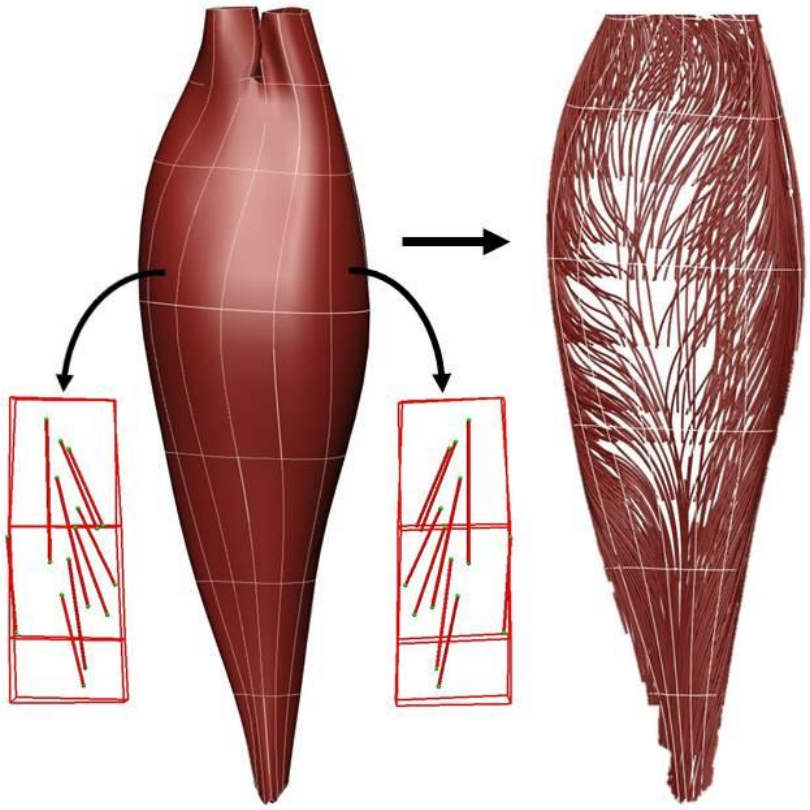

Figure 7: (Left) Bi-pennate muscle primitive used to construct a whole gastrocnemius muscle; and (right) complete fitted fibre field within whole muscle.

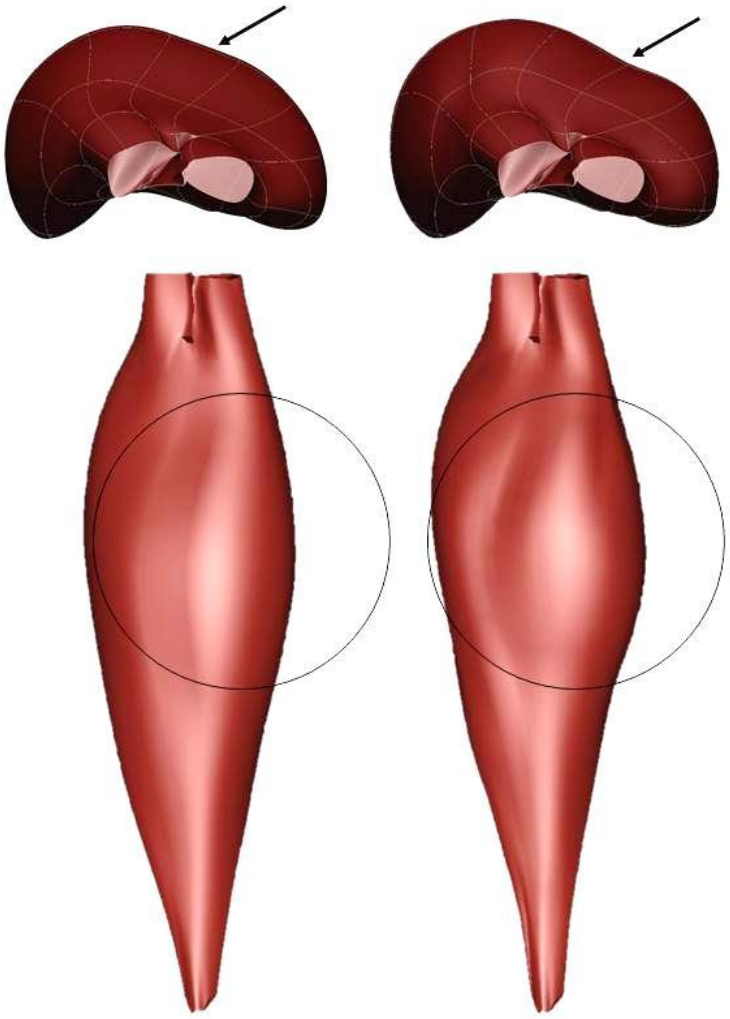

Figure 8: Ultrasound informed muscle in (left) relaxed state and (right) fully contracted state. The top shows an axial view and the bottom shows a posterior coronal view.

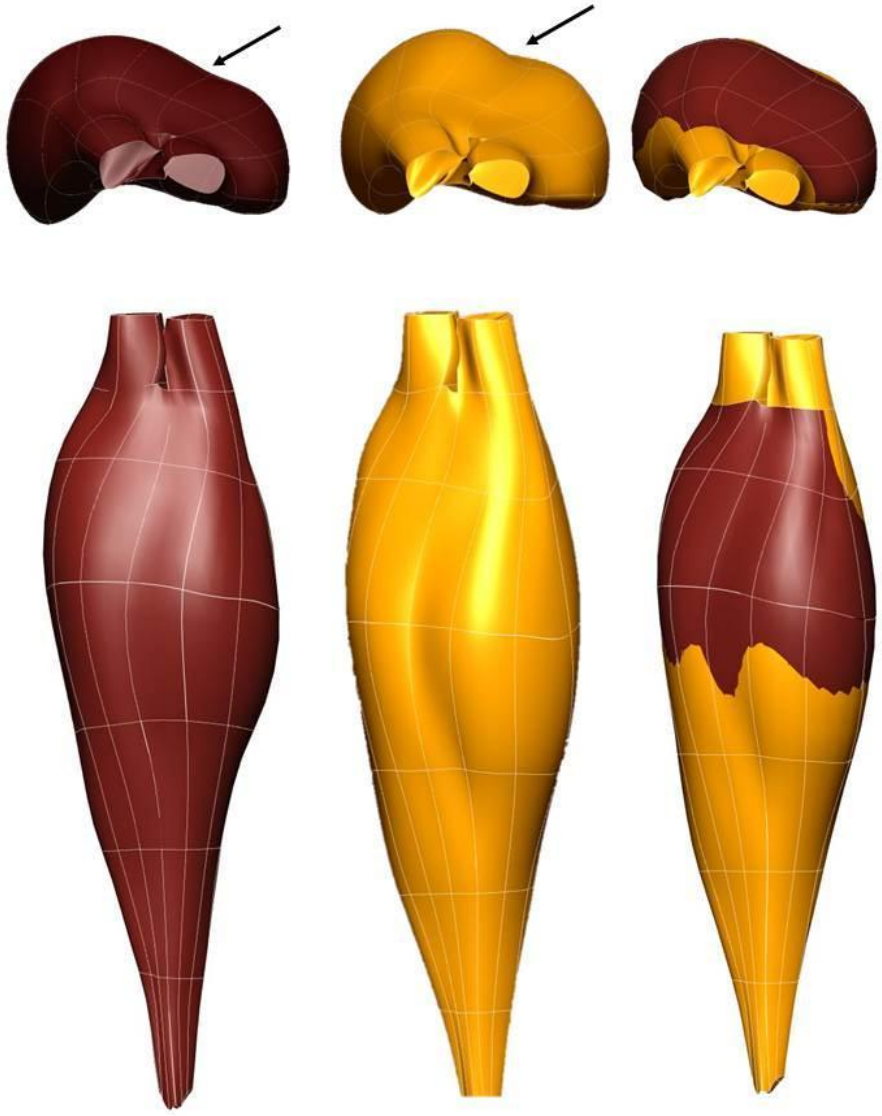

Figure 9: (left) Fully contracted muscle derived from ultrasound, (middle) DWI and (right) overlaid. The top shows an axial view and the bottom shows a posterior view.

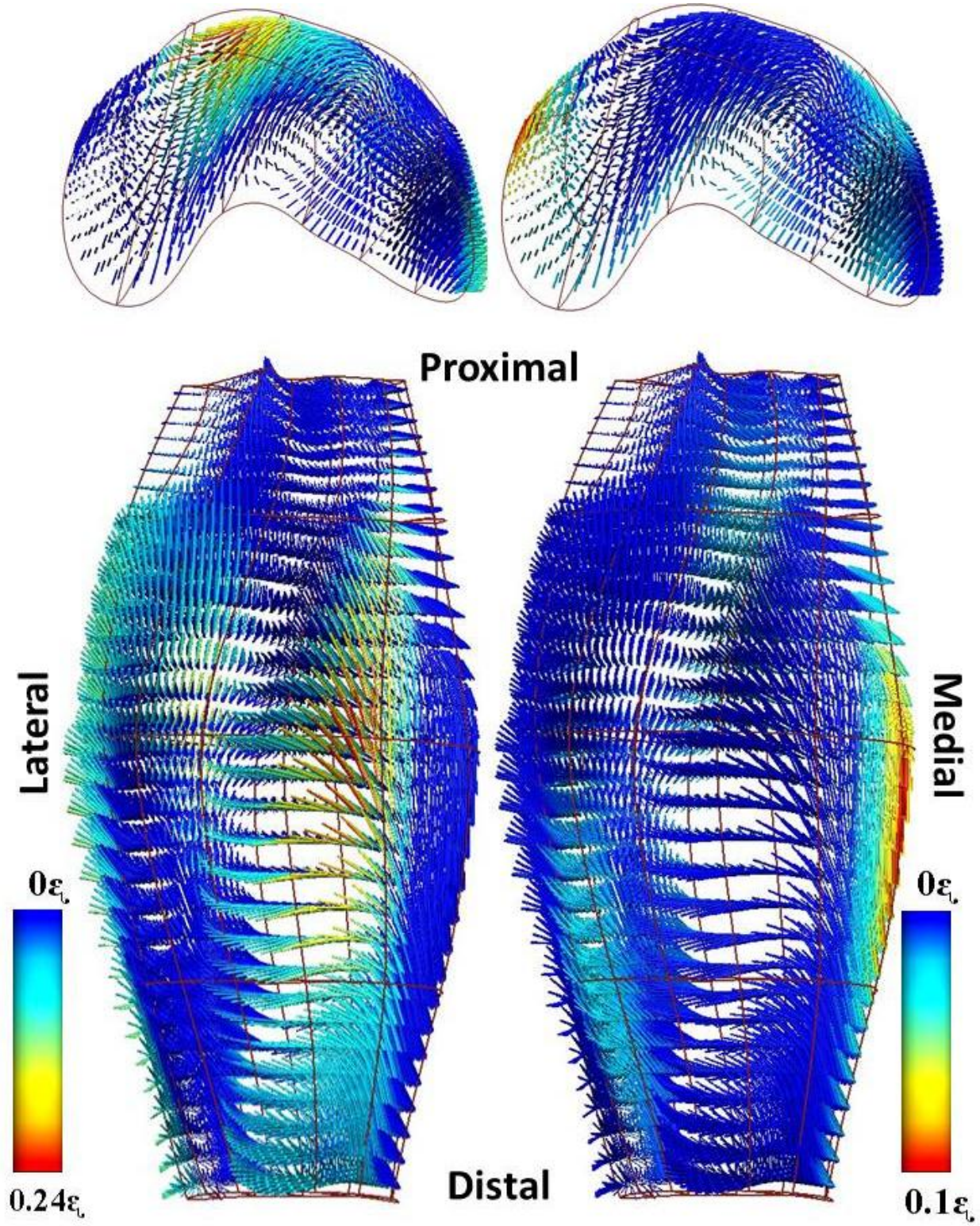

Figure 10: (left) Maximum principal compressive and (right) tensile strain from the (top) axial and (bottom) posterior views.

Tables:

Table 1: Subject statistics.

Subject	Age (Years)	Weight (kg)	Height (cm)	Leg length (cm)	Knee angle (º)
1	25	52	169	39.5	78
2	21	76	181	38	72
3	18	68	175	39.5	90
4	31	54	168	38.5	76
mean	24.6	60.6	171.6	38.8	79.0
SD	5.2	10.8	6.4	0.7	6.7
min	18	52	165	38	72
max	31	76	181	39.5	90

Table 2: Subject tensions during muscle elongation.

	FORCE (N)			
Muscle Stretche %	**Subject 1**	**Subject 2**	**Subject 3**	**Subject 4**
25.00%	1.5	2.8	0.8	0.3
50.00%	4.1	8.4	3.7	1.7
75.00%	8.5	19.6	11.3	6.3
100.00%	15.5	39.9	31.7	21.1

Table 3: Min/max tension, muscle length, muscle slack length and muscle stiffness for each subject.

	Subject 1	Subject 2	Subject 3	Subject 4
Tension min (N)	2.5	1.9	0.4	0.1
Tension max (N)	42.4	17.5	32.1	21.2
Length min (m)	0.4	0.4	0.4	0.4
length max	0.4	0.4	0.4	0.4
Alpha (m^{-1})	82.8	88.6	127.2	119.4
Slack length	0.3	0.3	0.4	0.4

Table 4: Fitted 'pole zero' parameters for all four subjects.

	Subject 1	**Subject 2**	**Subject 3**	**Subject 4**
scaling κ_{11} (MPa)	0.1	0.1	0.1	0.1
pole α_{11}	0.12755	0.656	0.3047	0.494
curvature β_{11}	1	1	1	1
scaling κ_{22}/ κ_{33} (MPa)	0.1	0.1	0.1	0.1
pole α_{22}/ α_{33}	0.8	0.8	0.8	0.8
curvature β_{22}/ β_{33}	1	1	1	1
Avg % error	0.73%	0.71%	0.56%	0.30%

2